

Interseismic deformation from Sentinel-1 burst-overlap interferometry: Application to the southern Dead Sea fault

Xing Li¹, Sigurjón Jónsson¹, and Yunmeng Cao¹

¹King Abdullah University of Science and Technology

November 22, 2022

Abstract

Interferometric Synthetic Aperture Radar (InSAR) data are increasingly being used to map interseismic deformation with ascending and descending-orbit observations allowing for resolving for the near-east and vertical displacement components. The north component has, however, been difficult to retrieve due to the limited sensitivity of standard InSAR observations in that direction. Here we address this problem by using time-series analysis of along-track interferometric observations in burst-overlap areas of the TOPS imaging mode of the Sentinel-1 radar satellites. We apply this method to the southern part of the near-north striking Dead Sea transform fault to show that the ~ 5 mm/year relative motion is well recovered. Furthermore, the results indicate the locking depth of the fault decreases towards the south as it enters the transtensional Gulf of Aqaba basin. Our results show that time-series analysis of burst-overlap interferometric observations can be used to obtain meaningful interseismic deformation rates of slow-moving and northerly-striking faults.

Hosted file

supporting-information.docx available at <https://authorea.com/users/539560/articles/599954-interseismic-deformation-from-sentinel-1-burst-overlap-interferometry-application-to-the-southern-dead-sea-fault>

1
2 **Interseismic deformation from Sentinel-1 burst-overlap interferometry: Application**
3 **to the southern Dead Sea fault**

4 **Xing Li¹, Sigurjón Jónsson¹, Yunmeng Cao¹**

5 ¹King Abdullah University of Science and Technology (KAUST), Thuwal, Saudi Arabia.

6 Corresponding author: Sigurjón Jónsson (sigurjon.jonsson@kaust.edu.sa)

7 **Key Points:**

- 8 • Along-track Sentinel-1 burst-overlap interferometric time-series analysis is used to derive
9 mm/year interseismic velocities.
- 10 • The results indicate a decreasing locking depth of the southern Dead Sea fault towards
11 the Red Sea rift.
- 12
13
14
15
16
17
18
19
20
21
22
23
24
25
26
27
28
29
30
31
32

33 **Abstract**

34 Interferometric Synthetic Aperture Radar (InSAR) data are increasingly being used to map
35 interseismic deformation with ascending and descending-orbit observations allowing for
36 resolving for the near-east and vertical displacement components. The north component has,
37 however, been difficult to retrieve due to the limited sensitivity of standard InSAR observations
38 in that direction. Here we address this problem by using time-series analysis of along-track
39 interferometric observations in burst-overlap areas of the TOPS imaging mode of the Sentinel-1
40 radar satellites. We apply this method to the southern part of the near-north striking Dead Sea
41 transform fault to show that the ~ 5 mm/year relative motion is well recovered. Furthermore, the
42 results indicate the locking depth of the fault decreases towards the south as it enters the
43 transtensional Gulf of Aqaba basin. Our results show that time-series analysis of burst-overlap
44 interferometric observations can be used to obtain meaningful interseismic deformation rates of
45 slow-moving and northerly-striking faults.

46 **Plain Language Summary**

47 Measurements of interseismic deformation near plate-boundary faults are used to estimate how
48 large and how often major earthquakes are likely to occur and thus provide crucial input for
49 regional seismic hazard assessments. Geodetic GPS data have primarily been used for this task,
50 but increasingly Interferometric Synthetic Aperture Radar (InSAR) observations from satellites
51 have provided useful information, particularly in areas where GPS observations are scarce.
52 However, InSAR observations are only sensitive to the east and vertical components of
53 deformation, but not to the north component, and are thus of limited use to study northerly
54 striking earthquake faults. To address this problem, we combine advanced processing technique
55 called burst-overlap interferometry (BOI) with time-series analysis of a large data set to retrieve
56 millimeter per year details of north-south deformation. We apply this method to the north-
57 striking southern Dead Sea fault to show that the earthquake hazard decreases towards the south
58 as the fault enters Gulf of Aqaba and approaches the Red Sea rift. Our study demonstrates that
59 this method of BOI time-series analysis allows mapping the interseismic deformation of slow-
60 moving and north-striking faults.

61 **1 Introduction**

62 Geodetic measurements of interseismic deformation are used to estimate fault slip rates and
63 locking depths and thus provide key information for seismic hazard assessments. While geodetic
64 GNSS observations have been the main source of data for this purpose, InSAR has proven to be
65 useful in many areas, especially where GNSS data are scarce, such as in eastern Anatolia (e.g.,
66 Wright et al. 2001; Walters et al. 2011; Cavalié and Jónsson, 2014; Hussain et al., 2018) and
67 Tibet (e.g., Wright et al. 2004; Elliott et al., 2008; Cavalié et al., 2008). However, InSAR data
68 from polar-orbiting radar satellites have limited sensitivity to the north component of
69 displacement, meaning that standard InSAR observations are of little use for measuring
70 interseismic deformation near north-south striking fault systems.

71 To retrieve full 3D surface displacements from SAR imaging, azimuth pixel-offset tracking is
72 often used with both ascending and descending InSAR observations in cases when meter-scale
73 displacements have occurred, such as in large earthquakes (e.g., Fialko et al. 2001, Jónsson et al.,
74 2002; Wang and Jónsson, 2015; Akoglu et al., 2018). Similarly, azimuth split-beam
75 interferometry, also known as multiple aperture interferometry (MAI), can be used to retrieve the

76 horizontal displacements parallel to the satellite track (Bechor and Zebker, 2006; Jung et al.,
 77 2012), which in many cases performs better than the azimuth pixel-offset tracking (e.g., Elliott et
 78 al., 2007; Wang and Jónsson, 2015; Jónsson 2012). Still, both azimuth pixel-tracking and MAI
 79 do not resolve mm- and cm-scale displacements well, and are therefore not suitable for mapping
 80 interseismic deformation.

81 The two Sentinel-1 satellites operate in the so-called TOPS (Terrain Observation with
 82 Progressive Scan) acquisition mode, in which the antenna beam is rotated forward during
 83 scanning bursts at a constant rate. Multiple bursts from three sub-swaths are then stitched
 84 together to form an image. In burst-overlap areas between neighboring bursts, the ground is
 85 imaged twice from two different view directions (forward-looking and backward-looking). The
 86 Sentinel-1 TOPS data thus provide an increased squint angle diversity within burst overlap areas,
 87 and hence achieve a better resolution of the along-track horizontal motion than conventional
 88 split-beam interferometry. This technique was first used to improve the coregistration between
 89 reference and secondary images (Scheiber and Moreira, 2000; Yague-Martinez et al., 2016).
 90 However, with burst-overlap interferometry (BOI) much better along-track displacements can be
 91 obtained, i.e., by making a double-difference interferogram for the pixels within the burst-
 92 overlap areas. The usefulness of BOI observations has already been demonstrated in earth
 93 science applications, e.g., in cases of co-seismic and post-seismic deformation (e.g., Grandin et
 94 al., 2016, Jiang et al., 2017, Yague-Martinez et al., 2019).

95 We here propose to use time-series analysis of a large number of along-track BOI observations
 96 to map interseismic surface deformation. We apply the method on the Dead Sea transform fault,
 97 which is a roughly north-south oriented left-lateral continental transform fault between the north-
 98 moving Arabian plate and the Sinai plate in the eastern Mediterranean region. The fault has
 99 produced many devastating earthquakes in the past and good mapping of the interseismic
 100 deformation is important for quantifying how rapid its stress loading is, providing inputs for
 101 seismic hazard assessments. The long-term slip rate estimates of the Dead Sea fault from offset
 102 geological and archaeological structures (e.g., Ginat et al., 1998; Klinger et al., 2000; Niemi et
 103 al., 2001) broadly agree with GPS results of the relative plate motion. These studies infer slip
 104 rates of the central and southern parts of the Dead Sea transform fault in the range of 3.8-6.0
 105 mm/yr (e.g., McClusky et al., 2003; Wdowinski et al., 2004; Reilinger et al., 2006; Le Béon et
 106 al., 2008; Al-Tarazi et al., 2011; Sadeh et al., 2012; Masson et al., 2015; Saleh and Backer, 2015;
 107 Hamiel et al., 2018; Gomez et al., 2020). Estimates of the fault locking depth, however, range
 108 considerably and almost no information is available about the locking depth of the southernmost
 109 part of the Dead Sea fault in Gulf of Aqaba.

110 **2 Methods**

111 The double-difference interferograms of the BOI method are generated within the burst-overlap
 112 areas as follows:

$$113 \quad \Phi_{\text{ovl}} = (r_1 \times s_1^*) \times (r_2 \times s_2^*)^*$$

114 where r and s represent the reference and secondary images, indices 1 and 2 the forward- and
 115 backward-looking views, and the $*$ symbol denotes the conjugate of a complex number. We first
 116 geometrically align the reference and secondary images, use precise orbits
 117 (<https://qc.sentinel1.eo.esa.int>) for orbital and topographic corrections, and then multi-look the
 118 images by a factor of 20 in range and 4 in azimuth prior to the computation of the double-
 119 difference interferograms. In addition, an azimuth phase de-ramping is applied to remove the

120 azimuth phase ramp caused by Doppler Centroid variations (Yagüe-Martínez et al., 2016,
 121 Grandin, 2015). A spatial coherence mask with a threshold of 0.45 is then applied to discard
 122 unreliable phase values.

123 The key advantage of the double-difference BOI observations is that they are sensitive to
 124 horizontal ground motion in the along-track direction, as the common line-of-sight displacement
 125 component cancels out. The along-track displacement Δaz (in centimeters) is retrieved from the
 126 double-difference phase $\Delta\Phi_{\text{ovl}}$ (in radians) by:

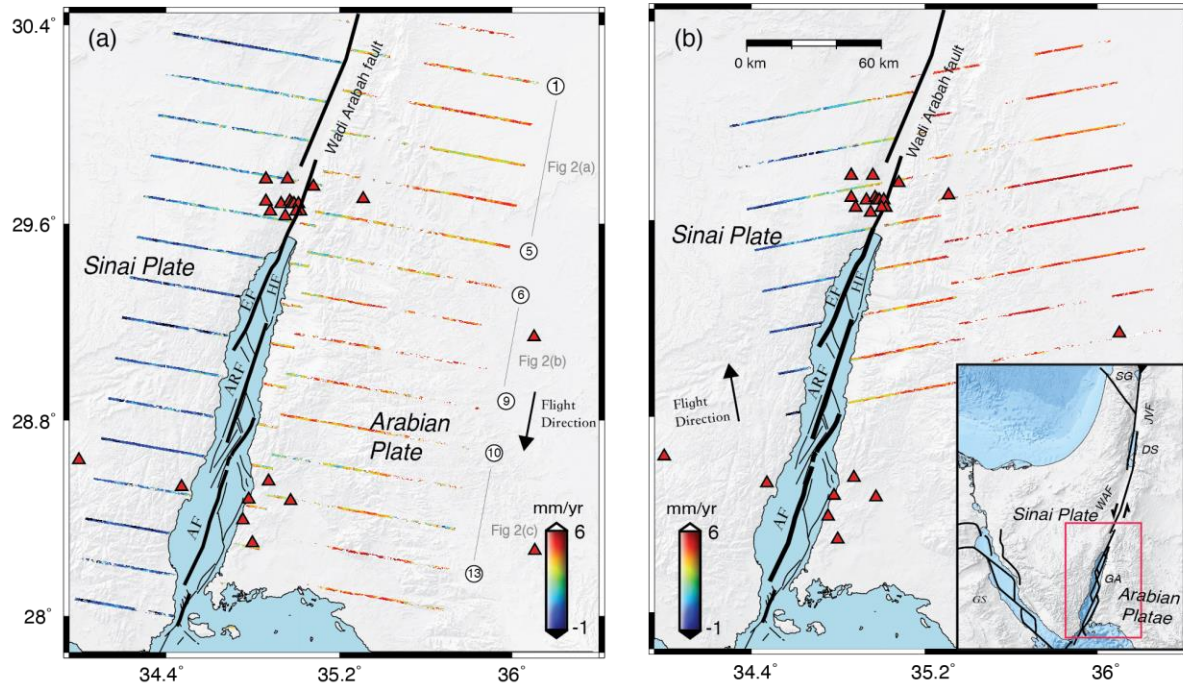
$$\Delta az = \Delta\Phi_{\text{ovl}} \frac{\lambda}{4\pi\Delta\psi_{\text{ovl}}}$$

127 where $\Delta\psi_{\text{ovl}} = \Delta\eta_{\text{ovl}}k_{\psi}$ is the squint angle difference between two consecutive overlaps, with
 128 $\Delta\eta_{\text{ovl}}$ and k_{ψ} representing the time separation between overlaps and the antenna beam steering rate
 129 of the Sentinel-1 data, respectively (Grandin et al., 2016). For the standard Sentinel-1
 130 interferometric wide swath (IW) TOPS imaging mode, the double difference phase is multiplied
 131 a factor ~ 21 cm/rad to obtain the along-track displacement (Grandin et al., 2016). Another
 132 advantage of the double-difference BOI observations is that the influence of the troposphere on
 133 the InSAR data is eliminated, but rapid spatial and temporal variations in the ionosphere can
 134 sometimes still induce artifacts in BOI observations.

135 To map horizontal along-track displacements near the Dead Sea transform fault, we use 161 and
 136 143 of Sentinel-1 images acquired from both ascending and descending orbits, respectively. The
 137 images span the time period from October 2014 to September 2020. We then combine multiple
 138 BOI with SBAS (Small Baseline Subset) time-series analysis to retrieve the horizontal
 139 displacement history for each pixel in the burst-overlap areas. This procedure both enhances the
 140 performance of the surface displacement estimation and allows for removing most of the
 141 ionospheric effects.

142 **3 Results**

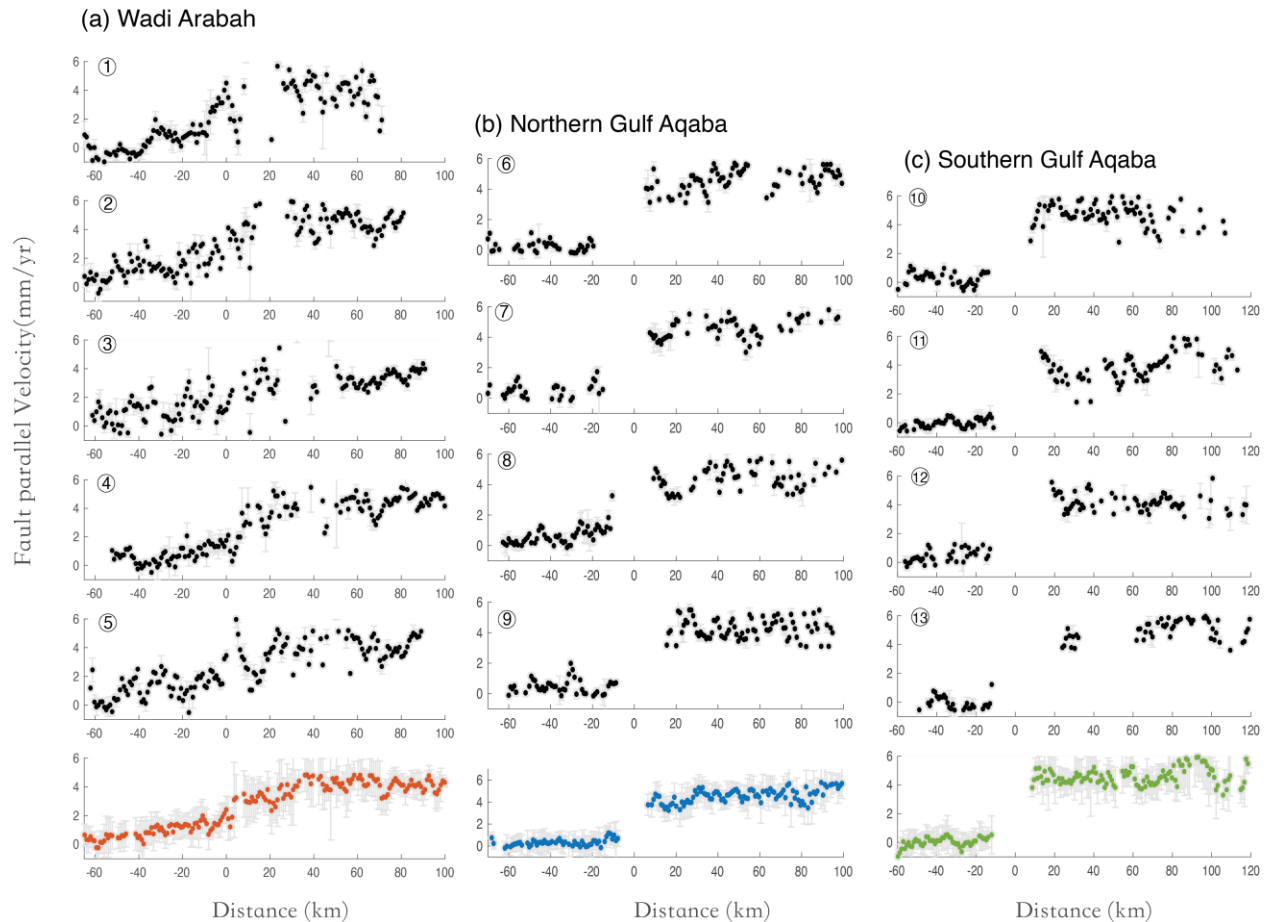
143 The derived along-track BOI velocities from both ascending and descending orbits show a clear
 144 and consistent velocity change across the Dead Sea fault from the western side to the eastern side
 145 of the fault (Fig. 1). The burst-overlap areas are about 1.5 km wide and 80 km long in each of the
 146 three sub-swaths of the Sentinel-1 IW imaging mode (here two sub-swaths were processed) and
 147 the distance between the burst-overlap areas is ~ 18 km. The burst overlap areas therefore
 148 spatially only cover $\sim 10\%$ of the ground and appear as narrow profiles in map view (Fig. 1). The
 149 derived along-track velocities are displayed with respect to the Sinai plate, i.e., the far-field
 150 velocities to the west are close to zero. We do this by averaging values at the far-western end of
 151 the profiles, within a 10 km*60 km window covering multiple burst-overlap areas, and then
 152 subtract the average value from the result. The strike of the southern Dead Sea transform fault is
 153 about $N10^{\circ}E$ and the descending BOI observations thus almost exactly map the fault-parallel
 154 motion, with the results showing left-lateral ground displacement rate of ~ 5 mm/yr. The
 155 ascending along-track observations also indicate significant left-lateral motion, but of somewhat
 156 lesser magnitude, presumably due to the $\sim 25^{\circ}$ difference between the ascending-orbit track
 157 direction and the strike of the Dead Sea fault.



158

159 Figure 1. Map of the southern Dead Sea transform fault showing the derived Sentinel-1 burst-overlap
 160 interferometry (BOI) along-track (see arrow) interseismic velocities for (a) descending-orbit track T21 and (b)
 161 ascending track T87. The velocities are shown with respect to stable Sinai plate. Positive values represent
 162 ground movement towards the north, i.e., the descending along-track velocity is reversed to show the left-
 163 lateral motion. Red triangles show GNSS station locations (Hamiel et al., 2018 and Gomez et al., 2020),
 164 arrows the along-track satellite flying direction, and circled numbers the BOI profiles shown in Fig. 2. EF:
 165 Eilat Fault; HF: Haql Fault; ARF: Aragonese Fault; AF: Arnona fault. The inset shows the study area location.
 166 GA: Gulf of Aqaba; DS: Dead Sea; WAF: Wadi Arabah Fault; JVF, Jordan Valley Fault; SG, Sea of Galilee.

167 We first inspect the deformation across the Wadi Arabah fault section of the Dead Sea fault,
 168 north of Gulf of Aqaba. Here we select five burst-overlap areas across the fault, from 30.4°N in
 169 the north to 29.6°N in the south, and plot each profile with the median values and 1 sigma
 170 uncertainties. Each median value is obtained by including all the along-track BOI observations
 171 with the same fault-perpendicular distance (Fig. 2). While individual BOI velocity profiles show
 172 considerable scatter, the average of these profiles indicate a consistent and smooth velocity
 173 transition from the Sinai plate in the west to the Arabian plate in the east, clearly showing the
 174 left-lateral motion across the fault (Fig. 2a, bottom).



175

176 Figure 2. The fault-parallel BOI velocities across the Dead Sea fault along each burst-overlap area (from Fig.
 177 1a) with median values plotted as black dots with 1 sigma uncertainties for the (a) Wadi Arabah fault, (b)
 178 northern Gulf of Aqaba, and (c) southern Gulf of Aqaba. The median value (black dot) is averaged with a
 179 1.2km*1.2km window and sampled with 1km spacing. The bottom rows show the stacked result from the
 180 profiles above.

181 Similarly, we use four burst-overlap profiles across the northern part of Gulf of Aqaba, stretching
 182 from 29.6°N in the north to 29°N near the southern end of Eilat fault, to assess the fault-parallel
 183 motion in this area. Here the left-lateral motion is also clearly visible, but more like a step
 184 function across the gap in the profile data, which corresponds to the gulf itself (Fig. 2b). In the
 185 southern gulf, four burst-overlap areas from 28.7°N to 28.2°N are shown and averaged indicating
 186 a similar sharp change across the gulf (Fig. 2c). The calculated stacked profile results for the
 187 three areas (bottom plots in Fig. 2) were derived by calculating the average of the individual
 188 burst-overlap profiles shown above, after eliminating outliers and locations with insufficient
 189 observations (i.e., less than 5 points). All the stacked profiles show clearly the ~5 mm/yr left-
 190 lateral motion but with notable differences in the profile shape across the fault.

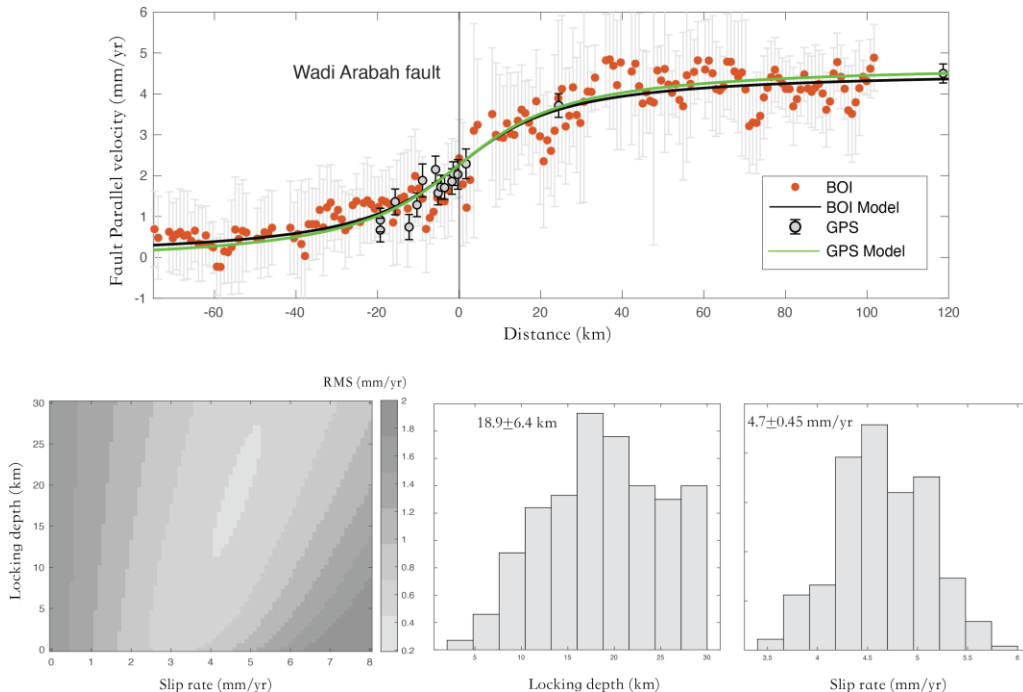
191 4 Modeling

192 We use the stacked fault-parallel velocity profiles of the descending-orbit BOI results to estimate
 193 the locking depth of the southern Dead Sea fault based on the widely-used 1D screw dislocation
 194 model (Weertman and Weertman 1964; Savage and Burford 1973). In this model, fault parallel
 195 velocity (v_0) is a function of perpendicular distance to the fault (x):

$$v = v_0 + \frac{s}{\pi} \tan^{-1}\left(\frac{x}{D}\right)$$

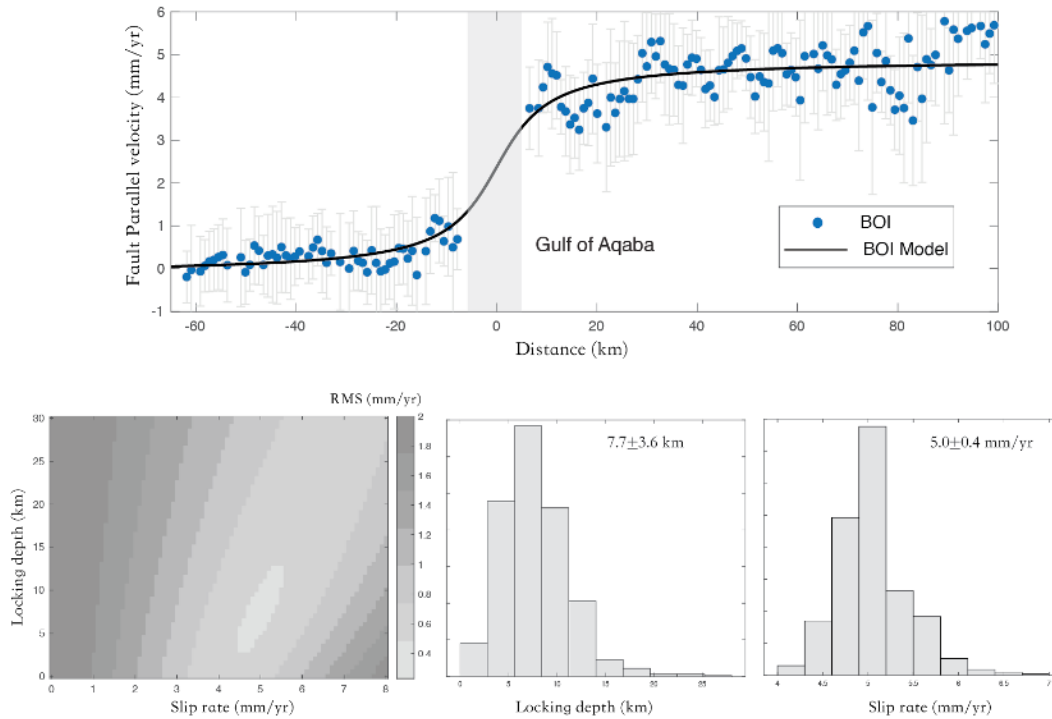
216 where v_0 defines a static offset, s and D are the long-term slip rate and locking depth, respectively. A grid-search method was applied to search for the best slip rate and locking depth values over ranges of 0-8 mm/yr and 0–30 km with 0.1 mm/yr and 0.5 km intervals. The modeling solved for three parameters: slip rate s , locking depth D , and the offset v_0 . The RMS (root mean square) misfit between the model prediction and observations for each combination of the parameters was calculated to find the optimal values of the slip rate and locking depth. The uncertainties of the obtained model parameters were then estimated by first perturbing the dataset with Gaussian noise and then searching for the optimal parameters of 1000 perturbed datasets, yielding a robust estimation of the model parameter uncertainties.

215 We separately estimate the locking depth for three different sections of the southern Dead Sea fault, i.e., for the Wadi Arabah fault in the north, and then the northern and southern Gulf of Aqaba. For each fault section, we use the average BOI time-series velocities from several burst-overlap areas (Fig. 2, bottom). For the Wadi Arabah fault, the smooth velocity transition from Sinai to Arabia yields a relative deep locking depth of 18.9 ± 6.4 km with a slip rate of 4.7 ± 0.45 mm/yr (Fig. 3). The fault-parallel BOI velocities in this area and the derived model parameters are in good agreement with published GPS results (Hamiel et al., 2018). When these GPS velocities from both near- and far-field campaign stations across the fault are used alone, they yield a similar locking depth of 19.9 ± 7.7 km and a slip rate of 5.0 ± 0.8 mm/yr (Fig. 3a), consistent with our BOI result.



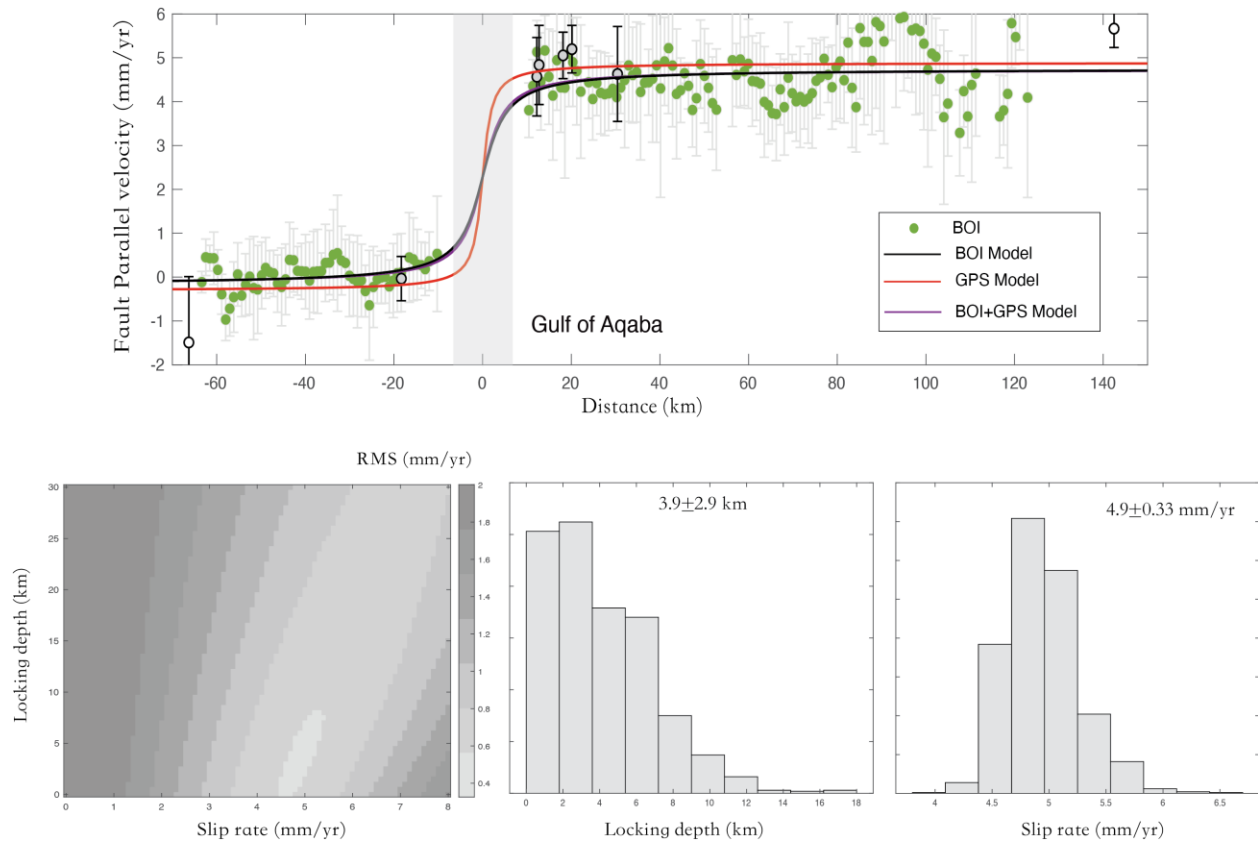
215
216 Figure 3. Observed fault-parallel BOI velocities (red dots) across the Wadi Arabah fault with 1σ uncertainties
217 (from Fig. 2a) in comparison with the screw-dislocation model prediction. Gray dots show fault-parallel GPS
218 velocities with 1σ uncertainties (Hamiel et al., 2018), shifted to match the BOI velocity reference, and the
219 model prediction using the GPS data alone (green line). The misfit (bottom left) shows the trade-off between
220 estimated locking depth and slip rate and the histograms indicate the model parameter uncertainties assessed
221 from the Monte Carlo simulation.

222 For the Gulf of Aqaba, we assume a single vertical fault extending from the southernmost tip of
 223 Arnona fault in the south to the northernmost tip of the gulf with a strike of 16° . We estimate a
 224 mean slip rate of 5.0 ± 0.4 mm/year with a locking depth of 7.7 ± 3.6 km for northern part of the
 225 gulf (Fig. 4), i.e., significantly shallower locking depth than for Wadi Arabah. This indicates that
 226 the moment accumulation rate of the fault decreases significantly as it enters the transtensional
 227 Gulf of Aqaba basin. The estimated locking depth of the southern Gulf of Aqaba is even
 228 shallower, or only 3.9 ± 2.9 km with a slip rate of 4.9 ± 0.33 mm/yr (Fig. 5). This means that we
 229 cannot exclude (at 2σ) the possibility that the fault is creeping at this location. Using the limited
 230 GPS results that have been published in the gulf area, and discarding far-field sites with large
 231 variations, we also obtain a very shallow locking depth of 1.5 km for the southern part of the gulf
 232 and a slip rate of 5.2 mm/yr. Combined, the BOI and GPS results yield a locking depth of 3.5 km
 233 and a slip rate of 4.9 mm/yr (Fig. 5). Overall, the results suggest that the locking depth of the
 234 southern Dead Sea fault gradually decreases as the fault extends into the Gulf of Aqaba and
 235 towards the active Red Sea rift zone.



236

237 Figure 4. Fault-parallel BOI velocities (blue dots) with 1σ uncertainties across the northern Gulf of Aqaba
 238 (from Fig. 2b) in comparison with the best screw-dislocation model prediction. The lower panels are as in Fig.
 239 3.



240

241 Figure 5. Fault-parallel BOI velocities (green dots) with 1σ uncertainties across the southern Gulf of Aqaba
 242 (from Fig. 2c) in comparison with GPS and model predictions (see text). Gray dots represent GPS
 243 observations with 1σ uncertainty (Gomez et al., 2020), while white GPS dots were dismissed from the
 244 analysis. The lower panels are as in Fig. 3.

245 5 Discussion and Conclusions

246 Our BOI results show a clear left-lateral movement focused on the southern Dead Sea fault of
 247 4.5-5 mm/yr, which is in agreement with both geologic and GPS estimates of the fault slip rate
 248 (e.g., Bartov et al., 1980; Le Béon et al., 2008; Hamiel et al., 2018; Gomez et al., 2020). The BOI
 249 velocities are not calibrated in any way by GPS data or other land-based measurements, i.e., they
 250 are derived solely from the Sentinel-1 BOI time-series analysis, and thus provide a new
 251 independent estimate of the slip rate of the southern Dead Sea fault. In addition, not only is the
 252 relative plate motion well recovered, details of the interseismic deformation near the fault are
 253 also resolved to less than 1 mm/yr (e.g., Fig. 3). This demonstrates, for the first time, that
 254 accurate interseismic velocities can be derived for slow-moving north-striking faults using
 255 Sentinel-1 BOI data alone when a large number of BOI observations is used.

256 Previous studies of the locking depth of the southern Dead Sea fault mostly focused on the
 257 segment north of the Gulf of Aqaba, due to lack of GPS sites near the gulf. Similar as with the
 258 slip rate results, our locking depth estimate north of the gulf in Wadi Arabah agrees well with
 259 published GPS results (e.g., Hamiel et al., 2018). Further south, we have limited GPS data to
 260 compare with. However, despite the lack of near-field data due to the offshore location of the
 261 fault in the gulf, the BOI results clearly indicate a sharper transition of the relative motion across
 262 the fault than in Wadi Arabah (Fig. 2). Our results thus suggest a decreasing locking depth from

263 the north into the gulf and towards the Red Sea rift. The estimated locking depths are much
264 lower than in Wadi Arabah, or 7.7 ± 3.6 km in the northern gulf and only 3.9 ± 2.9 km in the
265 southern gulf, meaning that we cannot exclude continuous creep (at 2σ) of the Arnona fault in
266 the south. The structure of the Gulf of Aqaba shows that it has experienced significant extension
267 as well as left-lateral slip. The active extension and normal faulting are evident by the stark
268 topographic contrast between the 900-1800 m deep gulf basins and the surrounding ~ 2000 m
269 high mountains. The gulf has thus been subject to significant crustal thinning and probably has
270 elevated heat flow that might explain the smaller locking depth. The decreasing locking depth
271 towards the south may also imply an increasing influence from the Red Sea rift, located just
272 south of the gulf. Whatever the explanation for the smaller locking depth is, the result indicates a
273 lower moment accumulation rate on this portion of the fault system and thus lower earthquake
274 hazard as compared to the fault north of the gulf.

275 Using six years of Sentinel-1 data from Oct. 2014 to Sep. 2020, our analysis and uncertainty
276 assessment assumes a constant deformation rate during the study period. If our BOI uncertainties
277 are underestimated, the level of confidence of the estimated model parameters could be too
278 optimistic (e.g., Duputel et al., 2014). However, the BOI uncertainties seem rather to be
279 overestimated, judging from the consistency with GPS (Fig. 3) and the smooth gradual velocity
280 changes along each derived velocity profile (Fig. 2, bottom), implying that our data errors and
281 model confidence levels are on the conservative side. Therefore, the limitations of the simple 1D
282 screw-dislocation model as well as the uncertainty of the exact fault location on the seafloor
283 within the gulf are probably more important. Fault mapping within the gulf has revealed en-
284 echelon fault patterns with over-lapping faults and pull-apart basins that are far from a single
285 straight fault strand in the middle of the gulf. In the northern gulf, for example, the Eilat and
286 Haql faults bound the Eilat basin on the western and eastern side, respectively, with each fault
287 near the opposing gulf coastlines (Ribot et al., 2020). The BOI results show more interseismic
288 deformation on the western coast (Fig. 4), indicating the deformation is rather focused on the
289 Eilat fault than the Haql fault. However, whichever the main active fault is, the deformation in
290 the gulf is much more focused than to the north in Wadi Arabah, signifying a smaller locking
291 depth.

292 We have demonstrated the applicability of BOI time-series analysis to map interseismic
293 deformation across slow-moving north-striking faults, like the southern Dead Sea fault. Without
294 external constraints, the BOI time-series results reveal a fault-parallel velocity of 4.5-5 mm/yr,
295 consistent with GPS observations, as well as details of the near-fault interseismic deformation
296 pattern. The results furthermore indicate that the fault locking depth decreases towards the south
297 as the fault enters Gulf of Aqaba and becomes closer to the Red Sea rift. The achievable ground
298 velocity accuracy depends on temporal coherence and the number of images used in the BOI
299 time-series analysis, and can become lower than 1 millimeter per year when more than hundred
300 images are combined.

301 **Acknowledgments**

302 This study was supported by King Abdullah University of Science and Technology (KAUST),
303 awards BAS/1/1353-01-01 and OSR-CRG2020-4335. This study was supported by King
304 Abdullah University of Science and Technology (KAUST), awards BAS/1/1353-01-01 and
305 OSR-CRG2020-4335. Sentinel-1 SAR images can be freely accessed from the Copernicus Open
306 Access Hub (<https://scihub.copernicus.eu>). Sentinel-1 interferograms are processed with

307 software GAMMA (Werner et al., 2001). GPS data is available through Hamiel et al. 2018 and
 308 Gomez et al., 2020. Figures are prepared using Generic Mapping Tools (Wessel et al., 2013) and
 309 MATLAB.

310 **References**

- 311 Akoglu, H. (2018). User's guide to correlation coefficients. *Turkish journal of emergency*
 312 *medicine*, 18(3), 91-93.
- 313 Al Tarazi, E., Abu Rajab, J., Gomez, F., Cochran, W., Jaafar, R., & Ferry, M. (2011). GPS
 314 measurements of near - field deformation along the southern Dead Sea Fault System.
 315 *Geochemistry, Geophysics, Geosystems*, 12(12).
- 316 Bartov, Y., Steinitz, G., Eyal, M., & Eyal, Y. (1980). Sinistral movement along the Gulf of
 317 Aqaba—its age and relation to the opening of the Red Sea. *Nature*, 285(5762), 220-222.
- 318 Bechor, N. B., & Zebker, H. A. (2006). Measuring two-dimensional movements using a single
 319 InSAR pair. *Geophysical research letters*, 33(16).
- 320 Cavalié, O., & Jónsson, S. (2014). Block - like plate movements in eastern Anatolia observed by
 321 InSAR. *Geophysical Research Letters*, 41(1), 26-31.
- 322 Cavalié, O., Lasserre, C., Doin, M. P., Peltzer, G., Sun, J., Xu, X., et al. (2008). Measurement of
 323 interseismic strain across the Haiyuan fault (Gansu, China), by InSAR. *Earth and Planetary*
 324 *Science Letters*, 275(3-4), 246-257.
- 325 Duputel, Z., Agram, P. S., Simons, M., Minson, S. E., & Beck, J. L. (2014). Accounting for
 326 prediction uncertainty when inferring subsurface fault slip. *Geophysical journal international*,
 327 197(1), 464-482.
- 328 Elliott, J. L., Freymueller, J. T., & Rabus, B. (2007). Coseismic deformation of the 2002 Denali
 329 fault earthquake: Contributions from synthetic aperture radar range offsets. *Journal of*
 330 *Geophysical Research: Solid Earth*, 112(B6).
- 331 Elliott, J. R., Biggs, J., Parsons, B., & Wright, T. J. (2008). InSAR slip rate determination on the
 332 Altyn Tagh Fault, northern Tibet, in the presence of topographically correlated atmospheric
 333 delays. *Geophysical Research Letters*, 35(12).
- 334 Fialko, Y., Simons, M., & Agnew, D. (2001). The complete (3-D) surface displacement field in
 335 the epicentral area of the 1999 Mw7. 1 Hector Mine earthquake, California, from space geodetic
 336 observations. *Geophysical research letters*, 28(16), 3063-3066.
- 337 Ginat, H., Enzel, Y., & Avni, Y. (1998). Translocated Plio-Pleistocene drainage systems along
 338 the Arava fault of the Dead Sea transform. *Tectonophysics*, 284(1-2), 151-160.
- 339 Gomez, F., Cochran, W. J., Yassminh, R., Jaafar, R., Reilinger, R., Floyd, M., et al. (2020).
 340 Fragmentation of the Sinai Plate indicated by spatial variation in present-day slip rate along the
 341 Dead Sea Fault System. *Geophysical Journal International*, 221(3), 1913-1940.
- 342 Grandin, R. (2015). Interferometric processing of SLC Sentinel-1 TOPS data. In FRINGE'15:
 343 Advances in the Science and Applications of SAR Interferometry and Sentinel-1 InSAR
 344 Workshop, Frascati, Italy.

- 345 Grandin, R., Klein, E., Métois, M., & Vigny, C. (2016). Three-dimensional displacement field of
346 the 2015 Mw8. 3 Illapel earthquake (Chile) from across-and along-track Sentinel-1 TOPS
347 interferometry. *Geophysical Research Letters*, 43(6), 2552-2561.
- 348 Hamiel, Y., Masson, F., Piatibratova, O., & Mizrahi, Y. (2018). GPS measurements of crustal
349 deformation across the southern Arava Valley section of the Dead Sea Fault and implications to
350 regional seismic hazard assessment. *Tectonophysics*, 724, 171-178.
- 351 Hussain, Z., Arslan, M., Malik, M. H., Mohsin, M., Iqbal, S., & Afzal, M. (2018). Integrated
352 perspectives on the use of bacterial endophytes in horizontal flow constructed wetlands for the
353 treatment of liquid textile effluent: phytoremediation advances in the field. *Journal of*
354 *environmental management*, 224, 387-395.
- 355 Jiang, H., Feng, G., Wang, T., & Bürgmann, R. (2017). Toward full exploitation of coherent and
356 incoherent information in Sentinel - 1 TOPS data for retrieving surface displacement:
357 Application to the 2016 Kumamoto (Japan) earthquake. *Geophysical Research Letters*, 44(4),
358 1758-1767.
- 359 Jónsson, S. (2012). Tensile rock mass strength estimated using InSAR. *Geophysical research*
360 *letters*, 39(21).
- 361 Jónsson, S., Zebker, H., Segall, P., & Amelung, F. (2002). Fault slip distribution of the 1999 M
362 w 7.1 Hector Mine, California, earthquake, estimated from satellite radar and GPS measurements.
363 *Bulletin of the Seismological Society of America*, 92(4), 1377-1389.
- 364 Jung, H. S., Lu, Z., & Zhang, L. (2012). Feasibility of along-track displacement measurement
365 from Sentinel-1 interferometric wide-swath mode. *IEEE Transactions on Geoscience and*
366 *Remote Sensing*, 51(1), 573-578.
- 367 Klinger, Y., Avouac, J. P., Dorbath, L., Karaki, N. A., & Tisnerat, N. (2000). Seismic behaviour
368 of the Dead Sea fault along Arava valley, Jordan. *Geophysical Journal International*, 142(3),
369 769-782.
- 370 Le Béon, M., Klinger, Y., Amrat, A. Q., Agnon, A., Dorbath, L., Baer, G., et al. (2008). Slip rate
371 and locking depth from GPS profiles across the southern Dead Sea Transform. *Journal of*
372 *Geophysical Research: Solid Earth*, 113(B11).
- 373 Masson, F., Hamiel, Y., Agnon, A., Klinger, Y., & Deprez, A. (2015). Variable behavior of the
374 Dead Sea Fault along the southern Arava segment from GPS measurements. *comptes rendus*
375 *geoscience*, 347(4), 161-169.
- 376 McClusky, S., Reilinger, R., Mahmoud, S., Ben Sari, D., & Tealeb, A. (2003). GPS constraints
377 on Africa (Nubia) and Arabia plate motions. *Geophysical Journal International*, 155(1), 126-138.
- 378 Niemi, T. M., Zhang, H., Atallah, M., & Harrison, J. B. J. (2001). Late Pleistocene and Holocene
379 slip rate of the northern Wadi Arava fault, Dead Sea transform, Jordan. *Journal of seismology*,
380 5(3), 449-474.
- 381 Reilinger, R., McClusky, S., Vernant, P., Lawrence, S., Ergintav, S., Cakmak, R., et al. (2006).
382 GPS constraints on continental deformation in the Africa - Arabia - Eurasia continental collision
383 zone and implications for the dynamics of plate interactions. *Journal of Geophysical Research:*
384 *Solid Earth*, 111(B5).

- 385 Ribot, M., Klinger, Y., Jónsson, S., Avsar, U., Pons-Branchu, E., Matrau, R., et al. (2020).
386 Active faults' geometry in the Gulf of Aqaba, southern Dead Sea fault, illuminated by multi
387 beam bathymetric data.
- 388 Sadeh, M., Hamiel, Y., Ziv, A., Bock, Y., Fang, P., & Wdowinski, S. (2012). Crustal
389 deformation along the Dead Sea transform and the Carmel Fault inferred from 12 years of GPS
390 measurements. *Journal of Geophysical Research: Solid Earth*, 117(B8).
- 391 Saleh, M., & Becker, M. (2015). New constraints on the Nubia–Sinai–Dead Sea fault crustal
392 motion. *Tectonophysics*, 651, 79-98.
- 393 Savage, J. C., & Burford, R. O. (1973). Geodetic determination of relative plate motion in central
394 California. *Journal of Geophysical Research*, 78(5), 832-845.
- 395 Scheiber, R., & Moreira, A. (2000). Coregistration of interferometric SAR images using spectral
396 diversity. *IEEE Transactions on Geoscience and Remote Sensing*, 38(5), 2179-2191.
- 397 Walters, R. J., Holley, R. J., Parsons, B., & Wright, T. J. (2011). Interseismic strain accumulation
398 across the North Anatolian Fault from Envisat InSAR measurements. *Geophysical research
399 letters*, 38(5).
- 400 Wang, T., & Jónsson, S. (2015). Improved SAR amplitude image offset measurements for
401 deriving three-dimensional coseismic displacements. *IEEE Journal of Selected Topics in Applied
402 Earth Observations and Remote Sensing*, 8(7), 3271-3278.
- 403 Wdowinski, S., Bock, Y., Baer, G., Prawirodirdjo, L., Bechor, N., Naaman, S., et al. (2004). GPS
404 measurements of current crustal movements along the Dead Sea Fault. *Journal of Geophysical
405 Research: Solid Earth*, 109(B5).
- 406 Weertman, J., & Weertman, J. R. (1964). Elementary dislocation theory. Macmillan.
- 407 Werner, C., Wegmüller, U., Strozzi, T., & Wiesmann, A. (2000). Gamma SAR and
408 interferometric processing software. In *Proceedings of the ers-envisat symposium*, Gothenburg,
409 Sweden (Vol. 1620, p. 1620).
- 410 Wessel, P., Smith, W. H., Scharroo, R., Luis, J., & Wobbe, F. (2013). Generic mapping tools:
411 improved version released. *Eos, Transactions American Geophysical Union*, 94(45), 409-410.
- 412 Wright, T. J., Parsons, B. E., & Lu, Z. (2004). Toward mapping surface deformation in three
413 dimensions using InSAR. *Geophysical Research Letters*, 31(1).
- 414 Wright, T., Parsons, B., & Fielding, E. (2001). Measurement of interseismic strain accumulation
415 across the North Anatolian Fault by satellite radar interferometry. *Geophysical Research Letters*,
416 28(10), 2117-2120.
- 417 Yagüe-Martínez, N., Prats-Iraola, P., Gonzalez, F. R., Brcic, R., Shau, R., Geudtner, D., et al.
418 (2016). Interferometric processing of Sentinel-1 TOPS data. *IEEE Transactions on Geoscience
419 and Remote Sensing*, 54(4), 2220-2234.
- 420 Yagüe-Martínez, N., Prats-Iraola, P., Pinheiro, M., & Jaeger, M. (2019). Exploitation of burst
421 overlapping areas of tops data. Application to sentinel-1. In *IGARSS 2019-2019 IEEE
422 International Geoscience and Remote Sensing Symposium* (pp. 2066-2069). IEEE.